

Towards Intrinsic Charge Transport in Monolayer Molybdenum Disulfide by Defect and Interface Engineering

Zhihao Yu^{1,†}, Yiming Pan^{2,†}, Yuting Shen³, Zilu Wang⁴, Zhun-Yong Ong⁵, Tao Xu³, Run Xin¹, Lijia Pan¹, Baigeng Wang², Litao Sun^{3,*}, Jinlan Wang⁴, Gang Zhang⁵, Yong Wei Zhang⁵, Yi Shi^{1,*} & Xinran Wang^{1,*}

¹National Laboratory of Solid State Microstructures, School of Electronic Science and Engineering, National Center of Microstructures and Quantum Manipulation, Nanjing University, Nanjing 210093, P. R. China

²School of Physics, Nanjing University, Nanjing 210093, P. R. China

³SEU-FEI Nano-Pico Center, Key Laboratory of MEMS of Ministry of Education, Southeast University, Nanjing, 210096, P. R. China

⁴Department of Physics, Southeast University, Nanjing 211189, P. R. China

⁵Institute of High Performance Computing, 1 Fusionopolis Way, 138632, Singapore

† These authors contribute equally to this work.

* Correspondence should be addressed to X. W. (xrwang@nju.edu.cn) or Y. S. (yshi@nju.edu.cn) or L. S. (slt@seu.edu.cn).

Abstract

Molybdenum disulfide is considered as one of the most promising two-dimensional semiconductors for electronic and optoelectronic device applications. So far, the charge transport in monolayer molybdenum disulfide is dominated by extrinsic factors such as charged impurities, structural defects and traps, leading to much lower mobility than the intrinsic limit. Here, we develop a facile low-temperature thiol

chemistry to repair the sulfur vacancies and improve the interface, resulting in significant reduction of the charged impurities and traps. High mobility greater than $80\text{cm}^2 \text{V}^{-1} \text{s}^{-1}$ is achieved in backgated monolayer molybdenum disulfide field-effect transistors at room temperature. Furthermore, we develop a theoretical model to quantitatively extract the key microscopic quantities that control the transistor performances, including the density of charged impurities, short-range defects and traps. Our combined experimental and theoretical study provides a clear path towards intrinsic charge transport in two-dimensional dichalcogenides for future high-performance device applications.

Despite its great promise as a two-dimensional (2D) channel material for logic transistors^{1,2}, integrate circuits^{3,4} and photodetectors^{5,6}, the charge transport in monolayer of molybdenum disulfide (MoS₂) is still far away from the intrinsic limit. Theoretically, the phonon-limited mobility is $\sim 410\text{cm}^2\text{V}^{-1}\text{s}^{-1}$ at room temperature, and is weakly dependent on carrier density until $\sim 10^{13}\text{cm}^{-2}$, where electron-electron scattering starts to play important roles⁷. Experimentally however, very different behavior is observed regardless of the sample preparation method. Firstly, the electron mobility of backgated monolayer MoS₂ devices is limited to $\sim 40\text{cm}^2\text{V}^{-1}\text{s}^{-1}$ at room temperature, an order of magnitude lower than the phonon limit^{2, 8-10}. Secondly, the mobility is found to increase with carrier density even beyond 10^{13}cm^{-2} (Ref. 2, 9). Thirdly, at low carrier density, the charge transport is dominated by hopping mechanism^{11, 12}. Fourthly, a metal-insulator transition (MIT) is observed at high carrier densities on the order of 10^{13}cm^{-2} , but the underlying mechanism remains debated^{2, 8, 9}. These observations clearly point to the existence of extrinsic factors that dominate charge transport in monolayer MoS₂. Charged impurities (CI)^{2, 13}, short-range defects¹¹ and localized states^{11, 14, 15}, among others, are believed to strongly influence electron transport. However, a comprehensive physical picture that explains all of above-mentioned transport phenomena and provides quantitative and microscopic insights into the impurities is still lacking.

Due to its atomic thickness, electrons in monolayer MoS₂ are more susceptible to impurities both inside MoS₂ and at the dielectric interface. Therefore, the engineering of defects and interface represents a logical route to further improve MoS₂ device performance. Recently, the use of thiol-terminated SiO₂ (Ref. 16), boron nitride¹⁷, and suspended structure¹⁸ were found to improve the mobility of monolayer MoS₂ devices by several folds, showing the importance of interface. However, their mobility values

are still much lower than the intrinsic limit, indicating that other sources of impurities, most likely inside MoS₂, are still present.

In this work, we show that sulfur vacancies (SVs), which are the main type of intrinsic defects in MoS₂ (Ref. 11), can be effectively repaired by (3-mercaptopropyl)trimethoxysilane (MPS) under mild annealing, resulting in significant reduction of CI and short-range scattering. Monolayer MoS₂ with both sides treated by MPS exhibits a record-high mobility greater than 80cm²V⁻¹s⁻¹ (300cm²V⁻¹s⁻¹) at room temperature (low temperature), much higher than untreated samples. In addition, we show that MIT in MoS₂ is due to localized trap states, which can be modulated by improving the sample and interface quality. A theoretical model that takes into account the major scattering sources (phonon, CI and short-range defects) and localized charge traps is developed to quantitatively understand the scaling of mobility, conductivity and MIT in monolayer MoS₂. By fitting the experimental data, we are able to extract key microscopic quantities including the density of CI, short-range defects and charge traps, as well as derive a transport phase diagram for MoS₂. The quantitative information also allows us to discuss the possible origins of these extrinsic factors, which serve as the basis for further device optimization.

Repair of sulfur vacancies by thiol chemistry

The monolayer MoS₂ samples studied here are obtained by mechanical exfoliation from bulk crystals (Supplementary Fig. 1). A high density of SV exists in as-exfoliated MoS₂ as demonstrated in earlier works^{11, 19}. These defects, which can act as catalytic sites for hydrodesulfurization reactions^{20, 21}, are chemically reactive. Therefore, it is possible to repair the SV by thiol chemistry. Here, we choose a specific molecule MPS (Fig. 1 inset) for two reasons. (a) The S-C bond in MPS is

weaker than other thiol molecules like dodecanethiol due to the acidic nature of CH₃-O- groups, leading to a low energy barrier for the reaction²². (b) The trimethoxysilane groups in MPS react with the SiO₂ substrate to form a self-assembled monolayer²³ (SAM, Supplementary Fig. 2). The SAM layer can effectively passivate the MoS₂/SiO₂ interface, while the outstanding thiol group can also repair the SV on the bottom side of MoS₂, which is otherwise difficult to access. This unique property of MPS allows us to systematically compare three types of MoS₂ samples: as-exfoliated on SiO₂, top-side (TS) treated on SiO₂, and double-side (DS) treated. For the MPS treatment, we used a liquid-phase process²², followed by 350 °C annealing in forming gas to repair the SV (see Methods and Supplementary Fig. 3 for details of sample preparation and characterization).

We first study the reaction kinetics of SV and MPS by density functional theory (Fig. 1). The reaction can be described by $\text{HS}(\text{CH}_2)_3\text{Si}(\text{OCH}_3)_3 + \text{SV} \rightarrow \text{CH}_3(\text{CH}_2)_2\text{Si}(\text{OCH}_3)_3$ (Supplementary Fig. 4, Supplementary Movie 1), which is exothermic with the enthalpy change of -333.3kJ mol⁻¹ of MPS. The reaction process comprises of two steps with an energy barrier of 0.51eV and 0.22eV, respectively. In the first step (Supplementary Fig. 5), MPS chemically absorbs on to an SV through the sulfur atom, and then it cleaves the S-H bond and forms a thiolate surface intermediate. The dissociated H atom is bonded to a neighboring S atom. The second step involves cleavage of the S-C bond and hydrogenation of the thiolate intermediate to form the final product trimethoxy(propyl)silane (Supplementary Fig. 6). We note that the two-step process agrees well with earlier thiol absorption experiments on defective MoS₂^{20, 22}. The relatively low energy barriers also facilitate the reaction to happen at low temperature.

To quantify the effect of MPS treatment on sample quality, we perform

aberration-corrected transmission electron microscopy (TEM) on as-exfoliated and TS-treated monolayer MoS₂. Fig. 2 compares high-resolution TEM images of a typical as-exfoliated and TS-treated sample. The SVs can be clearly distinguished by analyzing the intensity profile¹¹ as shown in Supplementary Fig. 9. Statistical analysis (from more than 15 areas in each case) indicates that the density of SV is reduced from $\sim 6.5 \times 10^{13} \text{cm}^{-2}$ for the as-exfoliated samples to $\sim 1.6 \times 10^{13} \text{cm}^{-2}$ for the TS-treated samples (Supplementary Fig. 9c, d). Due to the difficulty in making TEM samples, we are not able to characterize the DS-treated MoS₂, where further reduction of SV is expected. During the course of TEM experiment, we have paid great attention to prevent the knock-on damage and lattice reconstruction caused by electron beam irradiation²⁴ by limiting the exposure time to less than 30s and the current density to below $10^6 \text{ e nm}^{-2} \text{S}^{-1}$ (Ref. 11). The SV generation rate induced by electron irradiation under our experimental conditions was very low, $\sim 5.6 \times 10^{10} \text{cm}^{-2} \text{S}^{-1}$ (Ref. 11). Therefore the SVs in Fig. 2 are believed to be intrinsic rather than induced by electron irradiation.

Electrical transport properties

Next, we systematically investigated the effect of MPS treatment on electrical transport properties of MoS₂. We fabricated backgated field-effect transistors (FETs) on as-exfoliated, TS-treated and DS-treated monolayer MoS₂ samples and carried out electrical measurements in high vacuum with standard four-probe technique, unless otherwise stated (see Methods for details of device fabrication and measurement). All the devices exhibited very small hysteresis at room temperature, which became even smaller as they were cooled down (Supplementary Fig. 10). Therefore, in the following we only present electrical data from the forward sweep.

Fig. 3a shows the four-probe conductivity $\sigma = \frac{I_{ds}}{\Delta V} \frac{L}{W}$ as a function of backgate

voltage V_g for three representative devices at room temperature (300K), where I_{ds} is the source-drain current; ΔV , L and W are the voltage difference, distance, and sample width between the two voltage probes, respectively. The MPS-treated samples show improved σ compared to the as-exfoliated one, indicating higher sample and interface quality. At carrier density $n=C_g V_g=7.1 \times 10^{12} \text{cm}^{-2}$ ($C_g=11.6 \text{nFcm}^{-2}$ is the gate capacitance for 300nm SiO_2 dielectrics), the DS-treated sample shows $\sigma = 1.52e^2 h^{-1}$ and field-effect mobility $\mu = \frac{d\sigma}{C_g dV_g} = 81 \text{cm}^2 \text{V}^{-1} \text{s}^{-1}$. To our best knowledge, this is the highest room-temperature field-effect mobility reported so far for monolayer MoS_2 regardless of the device geometry^{2, 8-10}.

To gain further insights into the charge transport physics, we performed variable-temperature electrical measurements down to 10K. Surprisingly, the three types of devices exhibit very different behavior (Fig. 3, Supplementary Fig. 11). For the as-exfoliated sample, σ monotonically decreases during cooling over the entire range of n , indicating an insulating behavior (Fig. 3d, Supplementary Fig. 11a). For the DS-treated sample, the transfer curves all intersect near $V_g=80\text{V}$ (corresponding to $n \sim 5.7 \times 10^{12} \text{cm}^{-2}$, Supplementary Fig. 11c), which is a signature of MIT. Metallic and insulating behaviors are observed down to the base temperature for $n > 6.6 \times 10^{12} \text{cm}^{-2}$ and $n < 3.5 \times 10^{12} \text{cm}^{-2}$ respectively. At intermediate n , the σ - T characteristics are not monotonic and MIT occurs within our experimental temperature range (solid symbols in Fig. 3f). For the TS-treated sample, MIT is observed for $n > 4.7 \times 10^{12} \text{cm}^{-2}$ (solid symbols in Fig. 3e), while insulating behavior is always observed at low temperatures (Fig. 3e, Supplementary Fig. 11b). As we shall see later, these distinct transport behaviors precisely reflect the quality of the MoS_2 and interface.

The scaling behavior of μ is also very different for the three samples (Fig. 3b-c). The as-exfoliated sample shows the lowest μ among the three samples. The μ - T curve

is not monotonic with a peak value of $31\text{cm}^2\text{V}^{-1}\text{s}^{-1}$ near 175K. On the other hand, μ monotonically increases for the MPS-treated samples upon cooling. For $T>100\text{K}$, $\mu \sim T^{-\gamma}$, where $\gamma=0.72$ and 0.64 for the DS-treated and TS-treated sample respectively. For $T<100\text{K}$, μ gradually saturates. At $T=10\text{K}$, $\mu=320\text{cm}^2\text{V}^{-1}\text{s}^{-1}$ for the DS-treated sample, which is ~ 3 (22) times higher than the TS-treated (as-exfoliated) one.

We stress that all the above-mentioned transport phenomena are reproducible among different samples. In Supplementary Fig. 12, we show three additional sets of data for two-terminal devices. Although the mobility is lower than their corresponding four-terminal counterparts due to contact resistance, all the key transport properties, including MIT, scaling of mobility and conductivity, are qualitatively reproduced.

Theoretical modeling of charge transport

Although some theories have been proposed to explain the mobility of monolayer MoS_2 ^{13, 25}, a more complete physical model remains to be developed to fully understand the charge transport. In particular, the model should establish the correlation between different transport regimes and the underlying microscopic scattering mechanisms, provide quantitative information about the samples, and project device performance based on realistic parameters.

We start by calculating the mobility of monolayer MoS_2 . According to Matthiessen's rule, the mobility for free carriers is expressed as

$$\mu_0(n, T)^{-1} = \mu_{ph}(T)^{-1} + \mu_{CI}(n, T)^{-1} + \mu_{sr}^{-1} \quad (1)$$

where μ_{ph} , μ_{CI} and μ_{sr} are mobility limited by phonons, CI, and short-range scatterings, respectively (the calculation of each term is described in Methods). The incorporation of μ_{sr} in our model is motivated by (i) TEM characterization that clearly shows the existence of short-range SV defects and (ii) the saturation of μ at

low temperatures. We do not consider surface optical phonon scattering because the relatively high energy of the SiO₂ phonon modes makes them irrelevant to the low-field mobility phenomenon considered here²⁵.

The experimentally measured “effective” field-effect mobility μ is not equal to the free-carrier mobility μ_0 , due to the presence of charge traps that limits the free carrier population. Recently, localized trap states within the bandgap have been observed in both exfoliated and CVD monolayer MoS₂ (Ref. 11, 14, 15). The impurity band from these trap states can introduce a mobility edge that strongly affects the charge transport²⁶. In a simple picture²⁷, transport is carried only by electrons in the extended states, *i.e.* states above the mobility edge. This model, which does not account for the hopping between the localized states, has been very successful in modeling organic FETs^{27, 28}. Here we adopt the same model to extract important physical quantities such as the density of CI (N_i) and trap states (N_{tr}), while avoiding the complexity of dealing with the energy-dependent mobility and percolation effects in hopping transport²⁷ (the detailed calculation is described in Methods). The model is further justified by its excellent agreement with the experimental data over a broad range of temperature and carrier density.

Discussion

With the above model, we can now quantitatively understand the obtained experimental data. The solid lines in Fig. 3 are the best fitting results using the parameters listed in Table 1. Remarkably, the scaling of mobility and conductivity with temperature and carrier density is well reproduced with a single set of parameters, suggesting that our model captures the essential physics. At low temperature and low carrier density, the calculated σ and μ are lower than experiments (Fig. 3b, d-f), presumably due to the omission of hopping transport in our model. Hence, the

discrepancy is the largest for the as-exfoliated sample (Fig. 3b, Fig. 3d) because N_{tr} is the highest.

The fitting parameters in Table 1 give considerable insights into the microscopic origin of impurities in MoS₂. In all of our samples, μ is much lower than μ_{ph} , indicating that phonon scattering does not play a significant role. Rather, the mobility is largely limited by CI and short-range scatterings. We notice that N_i and μ_{sr} are reduced by MPS treatment and are correlated for each sample, suggesting that CI partially shares the microscopic origin with short-range defects, most likely SV. CI also partially comes from the interface, as the DS-treated sample has much lower N_i than TS-treated one. For the DS-treated sample, N_i becomes comparable to that of SiO₂ substrate ($0.24\text{-}2.7 \times 10^{11} \text{cm}^{-2}$)²⁹⁻³¹, indicating that a large portion of SV is repaired. N_{tr} is also partially due to SVs as it can be reduced by MPS treatment. However, N_{tr} is an order of magnitude higher than N_i for all the samples, pointing to contributions from additional sources. This could be due to the ambient species absorbed between MoS₂ and SiO₂ during exfoliation, which act as charge traps as in the case of graphene^{29, 31, 32}.

For the MPS-treated samples, the high-temperature mobility is limited by CI, leading to the usual $T^{-\gamma}$ scaling behavior. Ref. 13 predicts $\gamma \sim 1$ for the range of carrier densities studied here. However, both short-range scattering (temperature independent) and thermal excitation from charge traps (which leads to the opposite trend since the density of electrons in the extended states n_c increases with temperature) can decrease the effective γ as observed here. Therefore, one cannot reliably infer the scattering mechanism solely by analyzing γ . When the charge traps become dominant (which usually happens at low temperature and low carrier density), the mobility even exhibits an insulating behavior as commonly observed in backgated devices^{2, 11, 12} and

in the as-exfoliated sample here (Fig. 3b).

The mobility increases with carrier density for all three samples from the combined effect of CI and charge traps (Fig. 3c). Below a threshold carrier density (equivalent to mobility edge), μ becomes negligible due to the localized nature of electrons in charge traps. The mobility edge is found to decrease with temperature (Supplementary Fig. 13) because of the thermal excitation of electrons to the extended states. At $T=80\text{K}$, the threshold density is about 2×10^{12} , 3×10^{12} and $5 \times 10^{12} \text{cm}^{-2}$ for the DS-treated, TS-treated and as-exfoliated sample respectively (Fig. 3c). These values are on the same order of magnitude with N_{tr} , further supporting the charge trap model.

Finally, we can also understand MIT in the framework of charge traps. Strong electron-electron correlation in 2D electron gas has been proposed to explain the MIT in monolayer MoS_2 which gives a universal threshold density $n_{MIT} \sim 10^{13} \text{cm}^{-2}$ (Ref. 2). In our experiments, however, n_{MIT} is apparently dependent on sample quality (Fig. 3). The MIT can be intuitively understood from Eq. 6 (Methods). When $n \ll N_{tr}$, the density of conducting electrons in the extended states (n_c) is exponentially dependent on temperature due to thermal activation, the temperature dependence of σ is dominated by n_c , showing thermally activated insulating behavior^{2, 11, 12, 14}. For even smaller n and T , transport is dominated by variable-range hopping because n_c can be ignored^{11, 14} (Fig. 4a). When $n \gg N_{tr}$, the Fermi level is far above the mobility edge and n_c is independent of temperature. Thus, the temperature dependence of σ is dominated by μ_0 , showing metallic behavior. Therefore, MIT occurs when $n \approx N_{tr}$. Using the trap and CI parameters of the DS-treated sample in Table 1, we numerically calculated $\sigma(n, T)$ (Eq. 6) and obtained the n and T of each critical point as in Fig. 3f. Fig. 4a shows the calculated transport phase diagram with metallic and insulating regions. Excellent agreement with experiment is achieved without any fitting

parameters, showing the consistency of our model. From Fig. 4a, n_{MIT} slowly increases with decreasing temperature, and converges to n_0 at $T=0K$. When $n>n_0$, metallic behavior is always expected. When $n<n_0$, MIT is always expected at finite temperature. Under realistic trap and CI parameters, n_0 is linearly proportional to, but slightly higher than N_{tr} (Fig. 4b, Supplementary Fig. 14). Therefore, n_0 can be used as a rough estimate of N_{tr} . After careful comparison with literature^{2, 9, 14, 33}, we find that the N_{tr} of our MPS-treated samples is indeed the lowest (Fig. 4b), consistent with the lowest observed n_0 .

From the above discussion, it is clear that the transport in current state-of-the-art monolayer MoS₂ samples is still limited by charge traps, CI and short-range defects. To reach the real potential of monolayer MoS₂ in high-performance devices, continuous improvement of sample and interface quality is still needed. In Fig. 4c, we project the room-temperature mobility as a function of N_{tr} in the ideal case, i.e. without CI and short-range scattering. The mobility at low carrier density is rapidly degraded by even a small N_{tr} . At a modest $n=7\times 10^{12}\text{cm}^{-2}$, N_{tr} has to be lower than $8.8\times 10^{11}\text{cm}^{-2}$, which is ~ 6 times lower than our DS-treated device, in order to achieve mobility greater than $400\text{cm}^2\text{V}^{-1}\text{s}^{-1}$.

In conclusion, we have shown that thiol chemistry is an effective approach to engineer the defects and interface in monolayer MoS₂ towards intrinsic charge transport. A physical model that includes charge traps and major scattering sources has been developed to comprehensively describe the charge transport in MoS₂ and to quantify the density of CI and charge traps in the samples. We believe that our model captures the essential charge transport physics for monolayer MoS₂ and can be readily extended to other 2D semiconductors³³⁻³⁵.

Methods

DFT calculations

DFT calculations were performed using the Vienna *ab initio* simulation package (VASP)^{36, 37}. Projector-augmented-wave (PAW)³⁸ potentials were used to describe ion-electron interactions, and the exchange correlation potential was represented by the local density approximation (LDA)³⁹. We used the climbing-image nudged elastic band (cNEB) method to locate the minimum energy paths and the transition states⁴⁰. The defective MoS₂ sheet was modeled by a 4 × 4 supercell of MoS₂ with a single SV. A k-point sampling of 5 × 5 × 1 was used for all the calculations.

MoS₂ sample preparation and MPS treatment

In this work, we exfoliated monolayer MoS₂ from natural bulk flakes (SPI Supplies). The as-exfoliated samples were directly exfoliated on 300nm SiO₂/Si substrate. Prior to device fabrication, the samples were annealed in a mixture of H₂/Ar at 350 °C to remove organic residue.

For the TS-treated samples, we first exfoliated monolayer MoS₂ on 300nm SiO₂/Si substrate, followed by annealing in a mixture of H₂/Ar at 350 °C to remove organic residue. The sample was then dipped in a fresh solution of 1/15 (v/v) MPS/dichloromethane for 24 hours in a dry glove box to grow MPS on MoS₂. After growth, the sample was taken out, rinsed thoroughly with dichloromethane and IPA and blown dry with N₂. Finally, the sample was annealed in a mixture of H₂/Ar at 350 °C for 20 minutes to finish the MPS treatment and remove the extra MPS on MoS₂ (Supplementary Fig. 3).

For DS-treated samples, the 300nm SiO₂/Si substrate was first subject to a 30-minute UV/ozone treatment to enhance surface hydrophilicity. The substrate was

then dipped in a 10% (v/v) MPS/dichloromethane solution for 12 hours in a dry glove box to grow MPS SAM. After the SAM growth, the substrate was sonicated in dichloromethane followed by thorough rinsing with dichloromethane and IPA and drying with N₂ (Supplementary Fig. 3). We then exfoliated monolayer MoS₂ on the SAM treated SiO₂/Si substrate. After exfoliation, the sample was dipped in a fresh solution of 1/15 (v/v) MPS/dichloromethane for 24 hours in a dry glove box to grow MPS on the top side of MoS₂, followed by thorough rinsing. Finally, the sample was annealed in a mixture of H₂/Ar at 350 °C for 20 minutes to finish the MPS treatment.

Device fabrication and electrical measurement

We used standard photolithography to pattern the electrodes of MoS₂ backgated FETs on 300nm SiO₂/Si substrates. Ti/Pd (20nm/20nm) was electron beam evaporated as the contact metal for source, drain and voltage probes, followed by lift-off. All devices were annealed at 350 °C in Ar to improve contacts. Electrical measurements were carried out by an Agilent B1500 semiconductor parameter analyzer in a close-cycle cryogenic probe station with base pressure $\sim 10^{-5}$ Torr. Prior to electrical measurements, a vacuum annealing at base pressure was performed to remove adsorbates and improve device performances⁴¹.

TEM characterizations

To prepare TEM samples, monolayer MoS₂ was first exfoliated on 300nm SiO₂/Si substrate. We then align-transferred the sample to a copper TEM grid by the PMMA-based transfer method described in Ref. 11.

The high-resolution TEM images were recorded in an image aberration-corrected

TEM (FEI Titan 80–300 at 80 kV) equipped with a charge-coupled device camera (GatanUltraScanTM 1000). The exposure time was 1s. Before recording, we set the third-order spherical aberration in the range of 1–6 μm and then we recorded the images under slightly underfocused. In order to minimize irradiation damage and prevent new SVs generating during normal imaging²⁴, we limited the total exposure time to less than 30 s and the current density to lower than $10^6 \text{ e/nm}^2/\text{S}$. A band-pass filter to the Fast Fourier Transformation of the original images was applied to enhance the visibility of the defects.

Theoretical modeling

The phonon-limited mobility is numerically calculated according to Ref. 7:

$$\mu_{ph}(T) = \begin{cases} \alpha_1 T^{-1}, T < 100\text{K} \\ \alpha_2 T^{-1.69}, T \geq 100\text{K} \end{cases} \quad (2)$$

where the coefficients $\alpha_1=2.625 \times 10^5 \text{ cm}^2 \text{KV}^{-1} \text{s}^{-1}$ and $\alpha_2=6.297 \times 10^6 \text{ cm}^2 \text{KV}^{-1} \text{s}^{-1}$ satisfy the boundary condition that $\mu_{ph}(300\text{K}) = 410 \text{ cm}^2 \text{V}^{-1} \text{s}^{-1}$ and that $\mu_{ph}(T)$ is continuous at 100K. The transition at 100K is due to the different phonon modes that limit the mobility⁷.

The CI-limited mobility is calculated by the model described in Ref. 13:

$$\mu_{CI}(n, T) = \frac{e}{\pi m \hbar^2 k_B T} \int_0^\infty f(E)[1 - f(E)] \Gamma_{imp}(E)^{-1} E dE \quad (3)$$

where $f(E)$ is the equilibrium Fermi-Dirac distribution function and Γ_{imp} is the electron momentum relaxation rate given by

$$\Gamma_{imp} = \frac{N_i}{2\pi\hbar} \int dk' \left| \phi_{k-k'}^{scr} \right|^2 (1 - \cos\theta_{kk'}) \delta(E_k - E_{k'}) \quad (4)$$

where $\phi_{|q|}^{scr}$ is the screened scattering potential for a single CI. The expression and

derivation for $\phi_{|q|}^{scr}$ can be found in Ref. 13. Physically speaking, $\phi_{|q|}^{scr}$ includes the effect of temperature-dependent charge polarizability on the electron screening of the charged impurity, which dominates the temperature dependence of the mobility at low and room temperature. The expression also implies that μ_{CI} is inversely proportional to N_i . Hence, from the fitting of the μ_{CI} to the total effective mobility data, we are able to quantify the N_i within the MoS₂. As an example, Supplementary Fig. 15 plots μ_{CI} as a function of T under $N_i=10^{12}\text{cm}^{-2}$.

The short-range-scattering-limited mobility μ_{sr} is a constant fitting parameter that does not depend on temperature or carrier density⁸.

To model the effect of charge traps, we assume the charge traps are uniformly distributed within ΔE_{tr} below the conduction band edge (Supplementary Fig. 16). We only consider shallow traps because the density of deep traps is at least an order of magnitude lower¹⁴, and that deep traps do not affect mobility and conductivity²⁷. The Fermi energy $E_F(n, T)$ is determined by

$$n = C_g V_g = \int_0^{+\infty} N_0 \frac{1}{e^{(E-E_F)/k_B T} + 1} dE + \int_{-\Delta E_{tr}}^0 \frac{N_{tr}}{\Delta E_{tr}} \frac{1}{e^{(E-E_F)/k_B T} + 1} dE \quad (5)$$

where $N_0 = \frac{2m^*}{\pi\hbar^2} = 3.8 \times 10^{14} \text{eV}^{-1} \text{cm}^{-2}$ is the density of states in the conduction band, and $m^* = 0.45m_e$ is the conduction band effective mass⁴². The density of conducting electrons in the extended states is

$$n_c(n, T) = \int_0^{+\infty} N_0 \frac{1}{e^{(E-E_F)/k_B T} + 1} dE \quad (6)$$

The conductivity is calculated by

$$\sigma(n, T) = en_c(n, T)\mu_0(n, T) \quad (7)$$

and the ‘‘effective’’ mobility is given by

$$\mu(n,T) = \mu_0(n,T) \frac{\partial n_c(n,T)}{\partial n} \quad (8)$$

References:

- 1 Liu, L., Kumar, S. B., Ouyang, Y. & Guo, J. Performance limits of monolayer transition metal dichalcogenide transistors. *IEEE Trans. Electron Devices* **58**, 3042–3047 (2011).
- 2 Radisavljevic, B., & Kis, A. Mobility engineering and a metal–insulator transition in monolayer MoS₂. *Nature Mater.* **12**, 815-820 (2013).
- 3 Wang, H. *et al.* Integrated circuits based on bilayer MoS₂ transistors. *Nano Lett.* **12**, 4674–4680 (2012).
- 4 Chuang, S. *et al.* MoS₂ P-type Transistors and Diodes Enabled by High Work function MoO_x Contacts. *Nano Lett.* **14**, 1337-1342 (2014).
- 5 Yu, W. *et al.* Highly efficient gate-tunable photocurrent generation in vertical heterostructures of layered materials. *Nature Nanotech.* **8**, 952-958 (2013).
- 6 Lopez-Sanchez, O., Lembke, D., Kayci, M., Radenovic, A., & Kis, A. Ultrasensitive photodetectors based on monolayer MoS₂. *Nature Nanotech.* **8**, 497-501 (2013).
- 7 Kaasbjerg, K., Thygesen, K. S. & Jacobsen, K. W. Phonon-limited mobility in n-type single-layer MoS₂ from first principles. *Phys. Rev. B* **85**, 115317 (2012).
- 8 Schmidt, H. *et al.* Transport properties of monolayer MoS₂ grown by chemical

- vapour deposition. *Nano Lett.* **14**, 1909-1913 (2014).
- 9 Baugher, B. W., Churchill, H. O., Yang, Y., & Jarillo-Herrero, P. Intrinsic Electronic Transport Properties of High-Quality Monolayer and Bilayer MoS₂. *Nano Lett.* **13**, 4212-4216 (2013).
 - 10 Liu, H. *et al.* Statistical study of deep submicron dual-gated field-effect transistors on monolayer chemical vapor deposition molybdenum disulfide films. *Nano Lett.* **13**, 2640-2646 (2013).
 - 11 Qiu, H. *et al.* Hopping transport through defect-induced localized states in molybdenum disulphide. *Nature Comm.* **4**, 2642 (2013).
 - 12 Ghatak, S., Pal, A. N., & Ghosh, A. Nature of electronic states in atomically thin MoS₂ field-effect transistors. *ACS Nano* **5**, 7707-7712 (2011).
 - 13 Ong, Z. Y., & Fischetti, M. V. Mobility enhancement and temperature dependence in top-gated single-layer MoS₂. *Phys. Rev. B*, **88**, 165316 (2013)
 - 14 Zhu, W. *et al.* Electronic transport and device prospects of monolayer molybdenum disulphide grown by chemical vapour deposition. *Nature Comm.* **5**, 3087 (2014).
 - 15 Ghatak, S., Mukherjee, S., Jain, M., Das Sarma, D. D., & Ghosh, A. Microscopic Origin of Charged Impurity Scattering and Flicker Noise in MoS₂ field-effect Transistors. <http://arxiv.org/abs/1403.3333> (2014).
 - 16 Najmaei, S. *et al.* Tailoring the physical properties of molybdenum disulphide monolayers by control of interfacial chemistry. *Nano Lett.* **14**, 1354–1361 (2014).
 - 17 Chan, M. *et al.* Suppression of thermally activated carrier transport in atomically

- thin MoS₂ on crystalline hexagonal boron nitride substrates. *Nanoscale* **5**, 9572-9576 (2013).
- 18 Jin, T., Kang, J., Kim, E. S., Lee, S., & Lee, C. Suspended single-layer MoS₂ devices. *J. Appl. Phys.* **114**, 164509 (2013).
- 19 Komsa, H. P., Kurasch, S., Lehtinen, O., Kaiser, U., & Krasheninnikov, A. V. From point to extended defects in two-dimensional MoS₂: Evolution of atomic structure under electron irradiation. *Phys. Rev. B* **88**, 035301(2013).
- 20 Wiegenstein, C. G., & Schulz, K. H. Methanethiol adsorption on defective MoS₂ (0001) surfaces. *J. Phys. Chem. B* **103**, 6913-6918(1999).
- 21 Peterson, S. L., & Schulz, K. H. Ethanethiol decomposition pathways on MoS₂ (0001). *Langmuir*, **12**, 941-945(1996).
- 22 Makarova, M., Okawa, Y., & Aono, M. Selective Adsorption of Thiol Molecules at Sulfur Vacancies on MoS₂ (0001), Followed by Vacancy Repair via S–C Dissociation. *J. Phys. Chem. C* **116**, 22411-22416 (2012).
- 23 Onclin, S., Ravoo, B. J., & Reinhoudt, D. N. Engineering Silicon Oxide Surfaces Using Self-Assembled Monolayers. *Angew. Chem. Int. Ed.* **44**, 6282-6304 (2005).
- 24 Komsa, H. P., Kotakoski, J., Kurasch, S., Lehtinen, O., Kaiser, U., & Krasheninnikov, A. V. Two-dimensional transition metal dichalcogenides under electron irradiation: defect production and doping. *Phys. Rev. Lett.* **109**, 035503(2012).
- 25 Ma, N., & Jena, D. Charge Scattering and Mobility in Atomically Thin Semiconductors. *Phys. Rev. X* **4**, 011043 (2014).

- 26 Ando, T., Fowler, A. B., & Stern, F. Electronic properties of two-dimensional systems. *Rev. Mod. Phys.* **54**, 437-672 (1982).
- 27 Xie, H., Alves, H., & Morpurgo, A. F. Quantitative analysis of density-dependent transport in tetramethyltetraselenafulvalene single-crystal transistors: Intrinsic properties and trapping. *Phys. Rev. B* **80**, 245305 (2009).
- 28 Salleo, A., Chen, T. W., Vokel, A. R., Wu, Y., Liu, P., Ong, B. S., & Street, R. A. Intrinsic hole mobility and trapping in a regioregular poly(thiophene). *Phys. Rev. B* **70**, 115311 (2004).
- 29 Burson, K. *et al.* Direct Imaging of Charged Impurity Density in Common Graphene Substrates. *Nano Lett.* **13**, 3576-3580 (2013).
- 30 Deshpande, A., Bao, W., Miao, F., Lau, C. N., & LeRoy, B. J. Spatially resolved spectroscopy of monolayer graphene on SiO₂. *Phys. Rev. B* **79**, 205411 (2009).
- 31 Martin, J. *et al.* Observation of electron–hole puddles in graphene using a scanning single-electron transistor. *Nature Phys.* **4**, 144-148 (2008).
- 32 Zhang, Y., Brar, V. W., Girit, C., Zettl, A., & Crommie, M. F. Origin of spatial charge inhomogeneity in graphene. *Nature Phys.* **5**, 722-726 (2009).
- 33 Li, L. *et al.* Black phosphorus field-effect transistors. *Nature Nanotech.* **9**, 372-377 (2014).
- 34 Fang, H., Chuang, S., Chang, T. C., Takei, K., Takahashi, T., & Javey, A. High-performance single layered WSe₂ p-FETs with chemically doped contacts. *Nano Lett.* **12**, 3788-3792 (2012).
- 35 Larentis, S., Fallahzad, B., & Tutuc, E. Field-effect transistors and intrinsic

- mobility in ultra-thin MoSe₂ layers. *Appl. Phys. Lett.* **101**, 223104 (2012).
- 36 Kresse, G.; Hafner, J. Ab Initio Molecular Dynamics for Open-Shell Transition Metals. *Phys. Rev. B* **48**, 13115–13118 (1993).
- 37 Kresse, G.; Furthmüller, J. Efficiency of Ab-Initio Total Energy Calculations for Metals and Semiconductors Using a Plane-Wave Basis Set. *Comput. Mater. Sci.* **6**, 15–50 (1996).
- 38 Blöchl, P. E. Projector Augmented-Wave Method. *Phys. Rev. B* **50**, 17953–17979 (1994).
- 39 Ceperley, D. M. Ground State of the Electron Gas by a Stochastic Method. *Phys. Rev. Lett.* **45**, 566–569 (1980).
- 40 Henkelman, G.; Uberuaga, B. P.; Jónsson, H. A Climbing Image Nudged Elastic Band Method for Finding Saddle Points and Minimum Energy Paths. *J. Chem. Phys.* **113**, 9901 (2000).
- 41 Qiu, H., Pan, L., Yao, Z., Li, J., Shi, Y., & Wang, X. Electrical characterization of back-gated bi-layer field-effect transistors and the effect of ambient on their performances. *Appl. Phys. Lett.* **100**, 123104 (2012).
- 42 Yoon, Y., Ganapathi, K. & Salahuddin, S. How good can monolayer MoS₂ transistors be? *Nano Lett.* **11**, 3768-3773 (2011).

END NOTES

Acknowledgements. This work was supported in part by Chinese National Key Fundamental Research Project 2013CBA01604, 2011CB922103, 2011CB707601, 2010CB923401, 2011CB302004; National Natural Science Foundation of China

61325020, 61261160499, 11274154, 61229401, 21173040, 21373045, 113279028, 61274114; National Science and Technology Major Project 2011ZX02707; Natural Science Foundation of Jiangsu Province BK2012302, BK20130055, BK20130016, BK2012024. J. W. acknowledges the computational resources provided by SEU and National Supercomputing Center in Tianjin.

Author Contributions. X. W and Y. S. conceived and supervised the project. Z. Y. and R. X. carried out sample preparation, device fabrication, electrical measurements and data analysis. Y. P., Z.-Y. O, B. W., G. Z. and Y. W. Z. performed modeling of charge transport. Y. S., T. X. and L. S. performed TEM characterizations and analysis. Z. W. and J. W. performed DFT calculations. L. P. devised the MPS treatment method. X. W., Y. S., L. S. and J. W. co-wrote the paper with all authors contributing to discussion and preparation of the manuscript.

Competing financial interests statement. The authors declare no competing financial interest.

Figure Captions

Figure 1 Kinetics and transient states of the reaction between a single SV and MPS. There are two energy barriers, the first one (0.51eV) is due to the S-H bond breaking, and the second one (0.22eV) is due to S-C bond breaking. (a)-(e) plots the initial, transient, and final states of the reaction. The SV in the initial state is illustrated by dashed line. The inset shows the chemical structure of MPS.

Figure 2 High-resolution aberration-corrected TEM images of (a) as-exfoliated and (b) TS-treated monolayer MoS₂ sample, showing the significant reduction of SV by MPS treatment. The SVs are highlighted by red arrows. The overlaid blue and yellow symbols mark the position of Mo and S atoms respectively. The scale bars are 1nm. Detailed intensity profile analysis and histogram of SV density are shown in Supplementary Fig. 9.

Figure 3 The effect of defect and interface engineering on monolayer MoS₂ charge transport. (a) Typical σ - V_g characteristics for as-exfoliated (black), TS-treated (blue), and DS-treated (red) monolayer MoS₂ at $T=300\text{K}$. (b) μ - T characteristics for the three devices at $n=7.1 \times 10^{12} \text{cm}^{-2}$. Solid lines are the best theoretical fittings. The dashed red line shows $T^{-0.72}$ scaling. (c) μ - n characteristics for the three devices at $T=80\text{K}$. Solid lines are the best theoretical fittings. (d)-(f) Arrhenius plot of σ (symbols) and theoretical fittings (lines) for the as-exfoliated (d), TS-treated (e) and DS-treated (f) MoS₂. From top to bottom, $n=7.0, 6.0, 5.0,$ and $4.0 \times 10^{12} \text{cm}^{-2}$ respectively. The critical points of the MIT are highlighted by solid symbols in (e) and (f). Insets in (d)-(f) show the cartoon illustration of the corresponding MoS₂ samples undergone different treatments.

Figure 4 Theory of charge transport in MoS₂. (a) Phase diagram of charge transport in monolayer MoS₂. The solid black line plots the calculated MIT critical points (using the parameters of DS-treated sample in Table 1) that separate the metallic and

insulating regimes. The red symbols are experimental MIT points extracted from Fig. 3f. The lower left corner of the phase diagram illustrates the hopping transport regime (not calculated). (b) The solid black line is the calculated n_0 as a function of N_{tr} using the parameters of DS-treated sample in Table 1. The MIT curves under different N_{tr} are plotted in Supplementary Fig. 14. The blue and red symbols are experimental points from the TS-treated and DS-treated samples in Fig. 3 respectively. We use the highest n that exhibit MIT as n_0 . The horizontal dashed lines are MIT critical density estimated from Ref. 2 and 9 respectively. The intersections with the solid line represent the estimate of N_{tr} in their devices (black arrows). (c) Theoretical calculation of μ as a function of N_{tr} at $T=300\text{K}$ without any CI or short-range scatterings (using the parameters of DS-treated sample in Table 1). From top to bottom, $n=2.0, 1.2, 0.7$ and $0.16 \times 10^{13} \text{ cm}^{-2}$ respectively. The phonon-limited value of $410 \text{ cm}^2 \text{ V}^{-1} \text{ s}^{-1}$ is recovered at $N_{tr}=0$.

Table 1 The fitting parameters in our theoretical model for the three devices in Fig. 3.

Figure 1

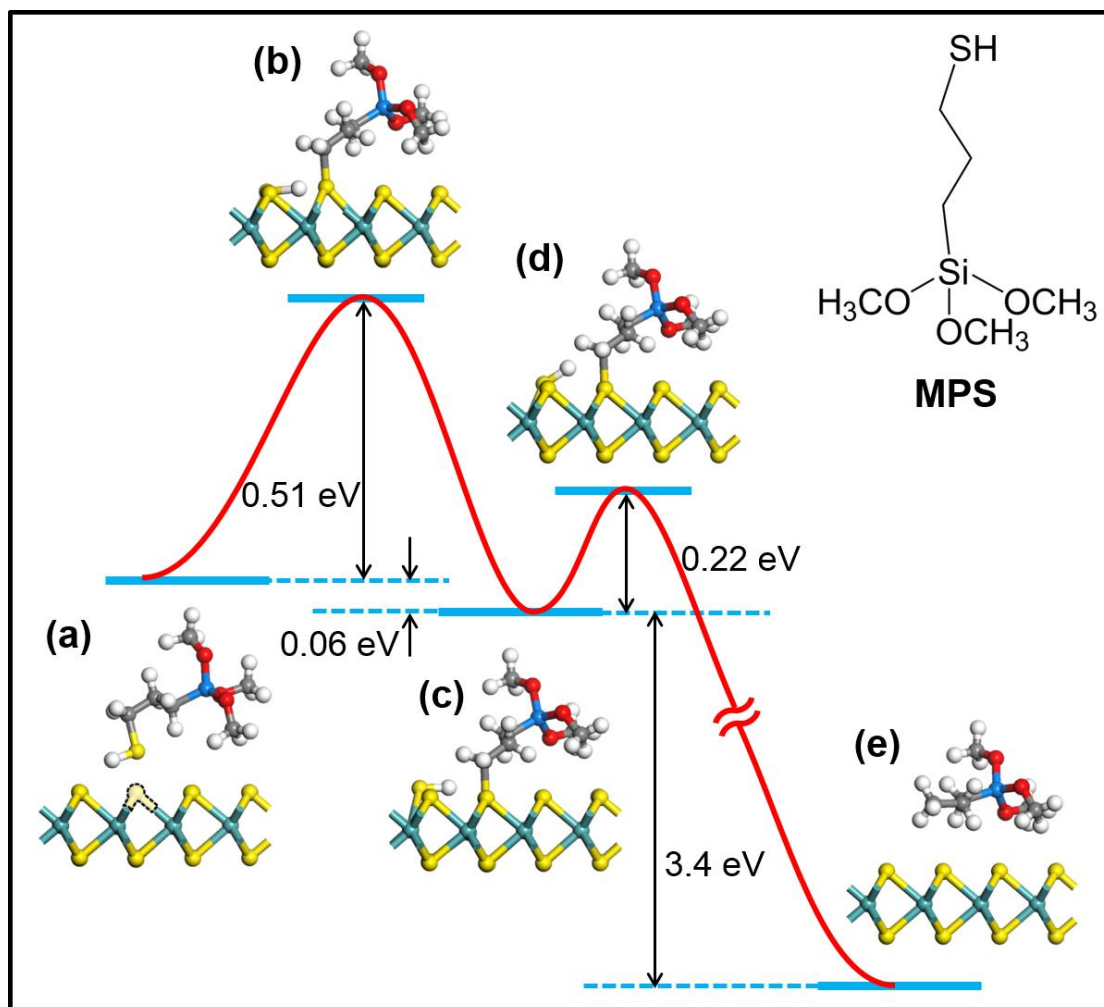


Figure 2

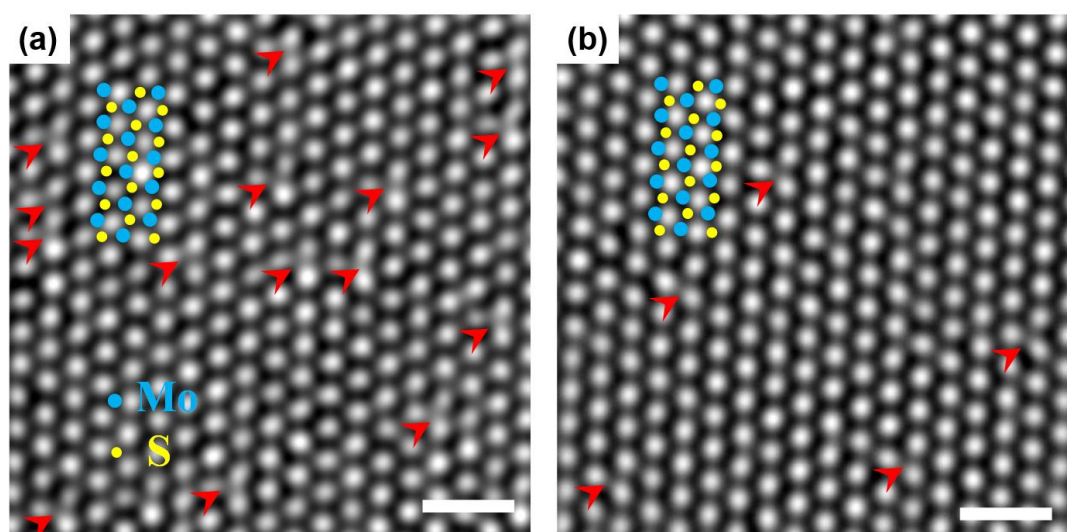


Figure 3

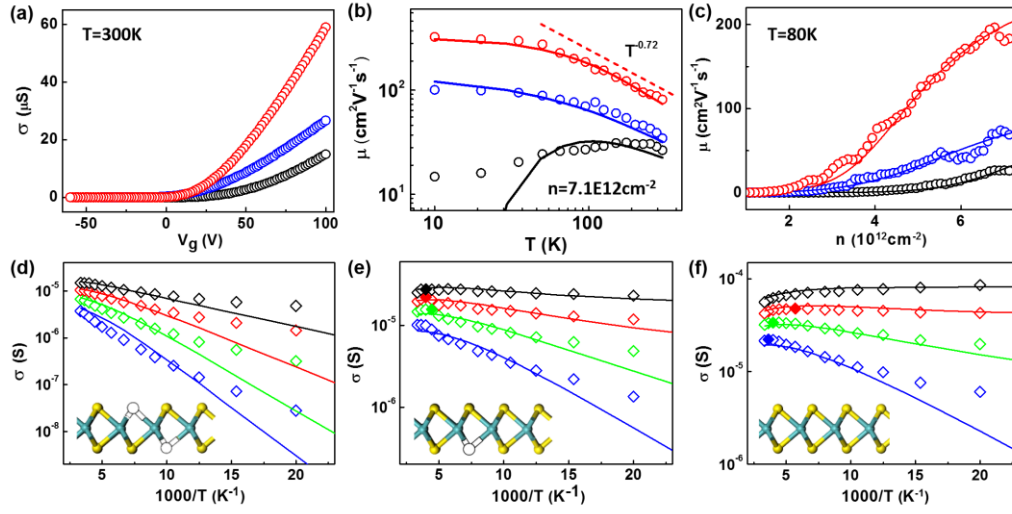


Figure 4

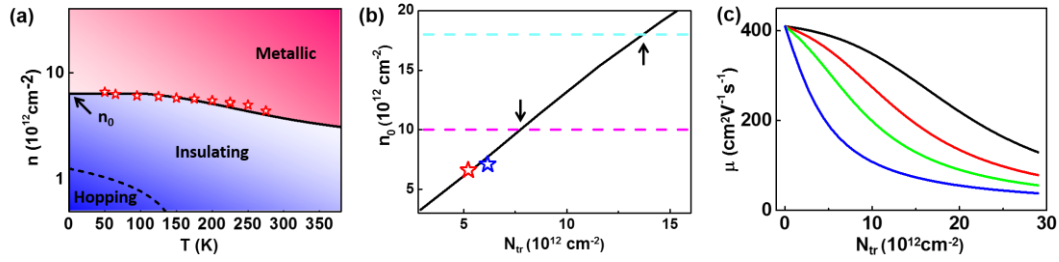
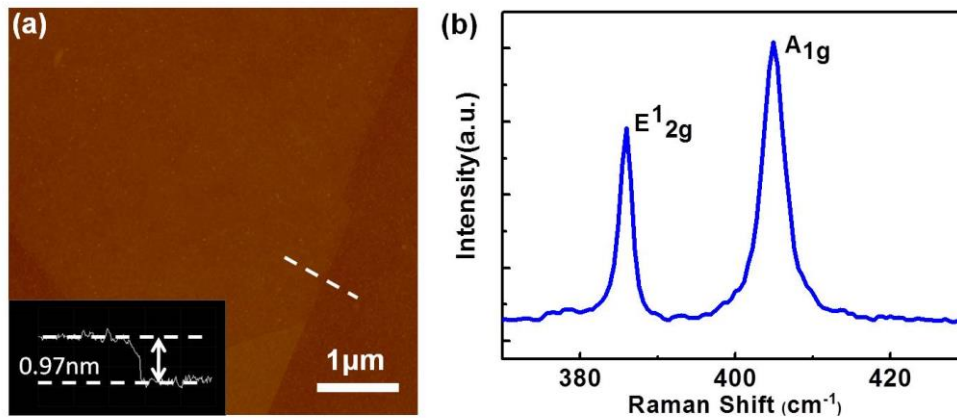
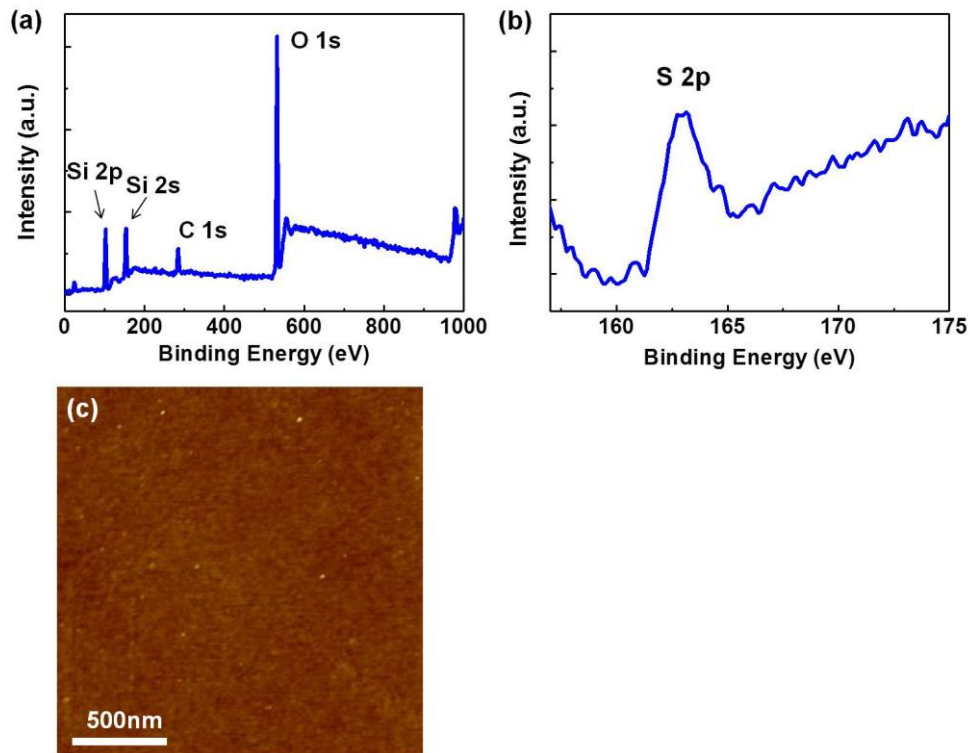


Table 1

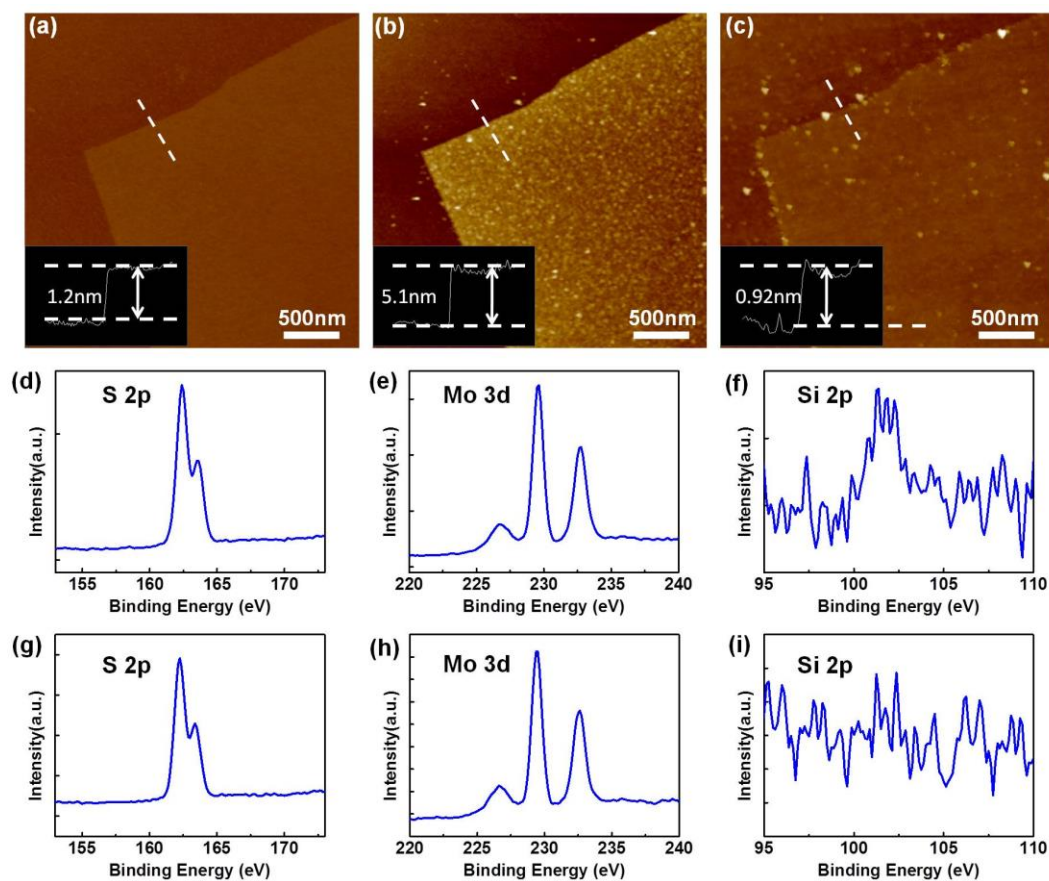
	as-exfoliated	TS-treated	DS-treated
N_i (10^{12}cm^{-2})	0.7	0.59	0.24
N_{tr} (10^{12}cm^{-2})	8.1	6.16	5.22
ΔE_{tr} (meV)	75	46	58
μ_{sr} ($\text{cm}^2\text{V}^{-1}\text{s}^{-1}$)	127	161	410

Supplementary Information:

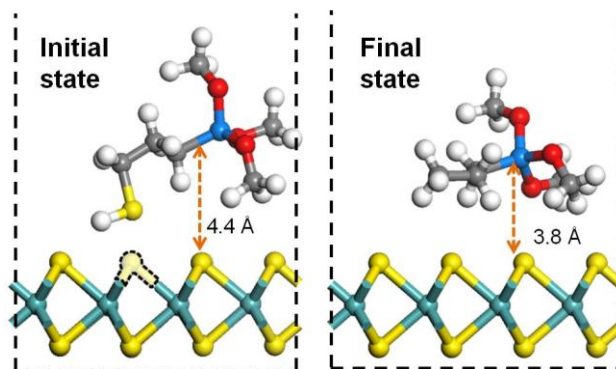
Supplementary Figure 1. Characterizations of monolayer MoS₂ studied in this work. We combine optical microscope, AFM and Raman spectroscopy to identify monolayer MoS₂ samples. (a) AFM image of a typical monolayer as-exfoliated MoS₂ sample on SiO₂/Si substrate. The height is ~1nm. (b) Raman spectrum of a typical monolayer MoS₂ sample. The position and relative intensity of the E¹_{2g} mode (386 cm⁻¹) and A_{1g} mode (405 cm⁻¹) confirm the monolayer nature¹.



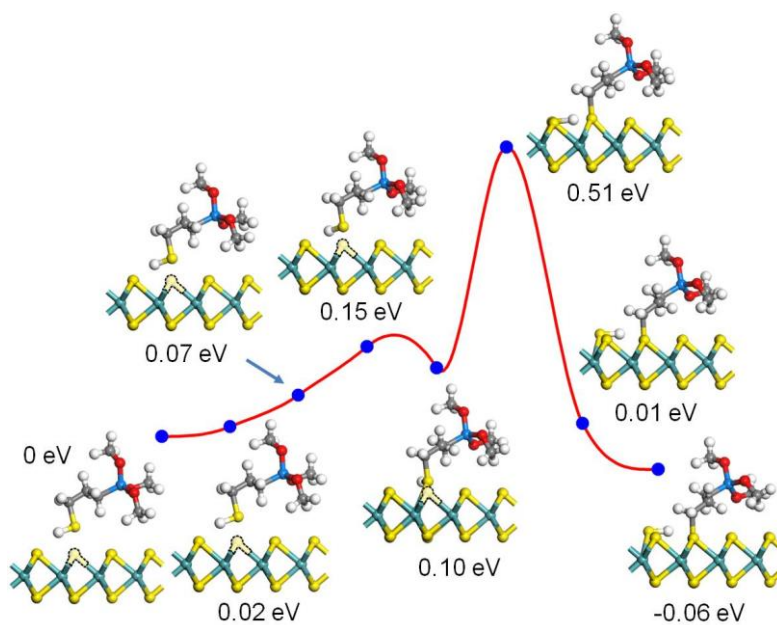
Supplementary Figure 2. Characterization of MPS grown on SiO₂ substrate. (a) X-ray photoelectron spectroscopy (XPS) survey scan of MPS SAM grown on 300nm SiO₂/Si substrate. The signal of Si, O, and C elements are most prominent. (b) High-resolution XPS scan near the S 2p region clearly showing the S signal from MPS. (c) AFM image of SiO₂ substrate after MPS SAM growth. The low roughness and good uniformity indicate the high quality of SAM growth.



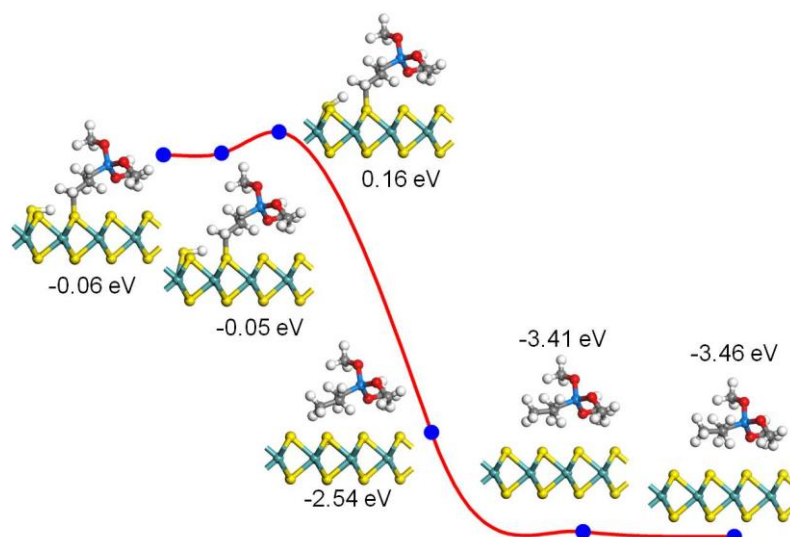
Supplementary Figure 3. Characterization of MoS₂ samples subject to MPS treatment. AFM images of the same monolayer MoS₂ sample (a) as-exfoliated on SiO₂/Si substrate, (b) after immersion in MPS solution and (c) after 350 °C annealing in H₂/Ar. The insets show the height of the sample at each stage. The apparent height of MoS₂ increases significantly after immersion in MPS, indicating that a thick layer of MPS is grown on top of the MoS₂. After the annealing step, the height of MoS₂ is restored, indicating that the extra MPS on MoS₂ is removed. (d)-(f) X-ray photoelectron spectroscopy (XPS) of MPS-treated MoS₂ and (g)-(i) as-exfoliated MoS₂. The existence of Si 2p peak in (f) clearly shows that the MPS grows on top of MoS₂.



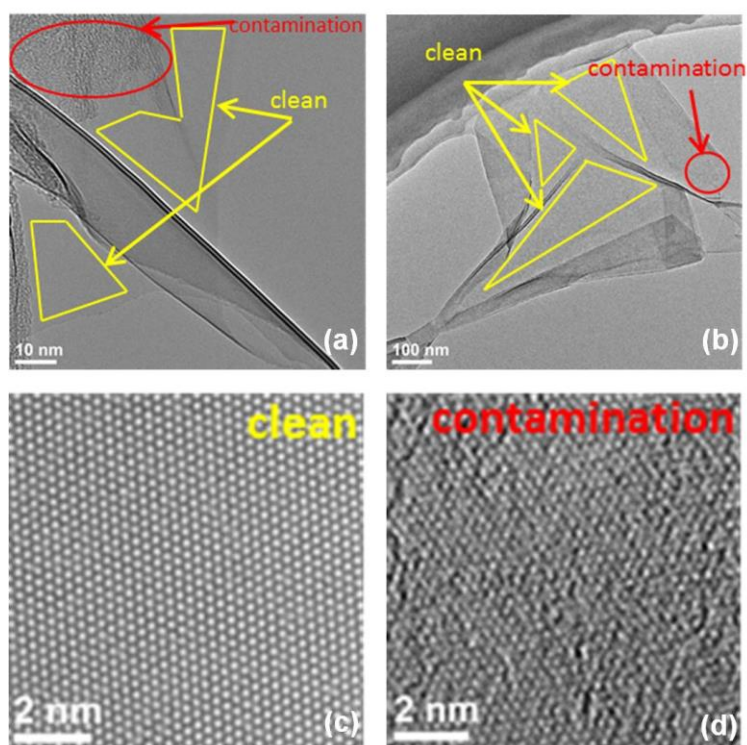
Supplementary Figure 4. Initial and final state of the chemical reaction in Fig. 1 of main text. The cyan, yellow, grey, white, red and blue balls denote Mo, S, C, H, O and Si atoms, respectively. The SV site is indicated by dashed line.



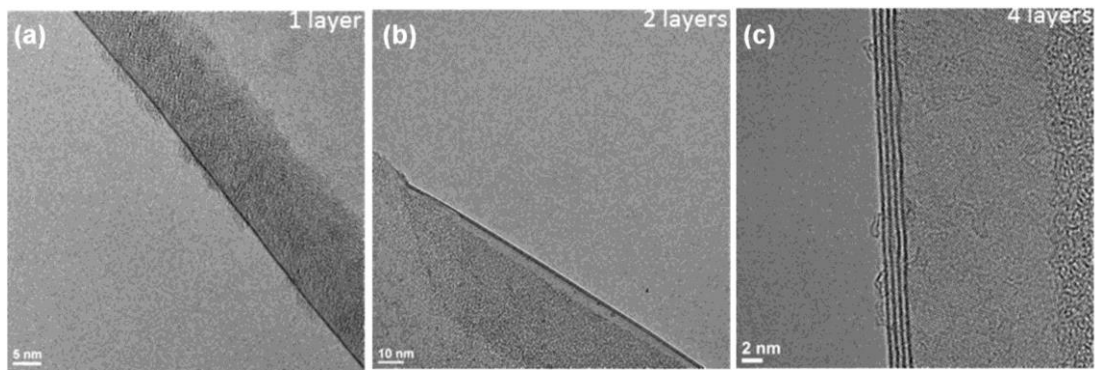
Supplementary Figure 5. Reaction kinetics and transient states of the S-H bond breaking step in the SV repair process.



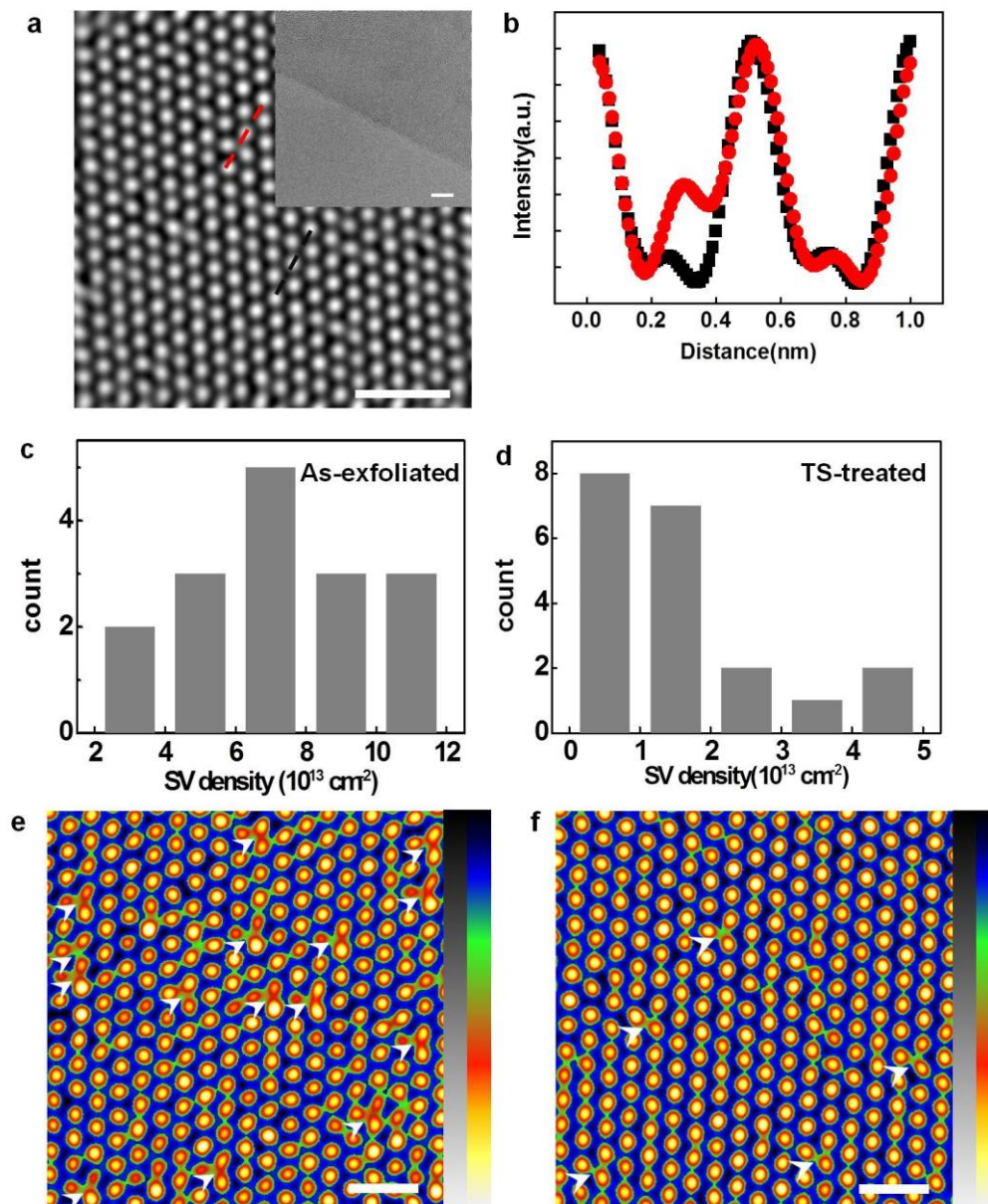
Supplementary Figure 6. Reaction kinetics and transient states of the S-C bond breaking step in the SV repair process.



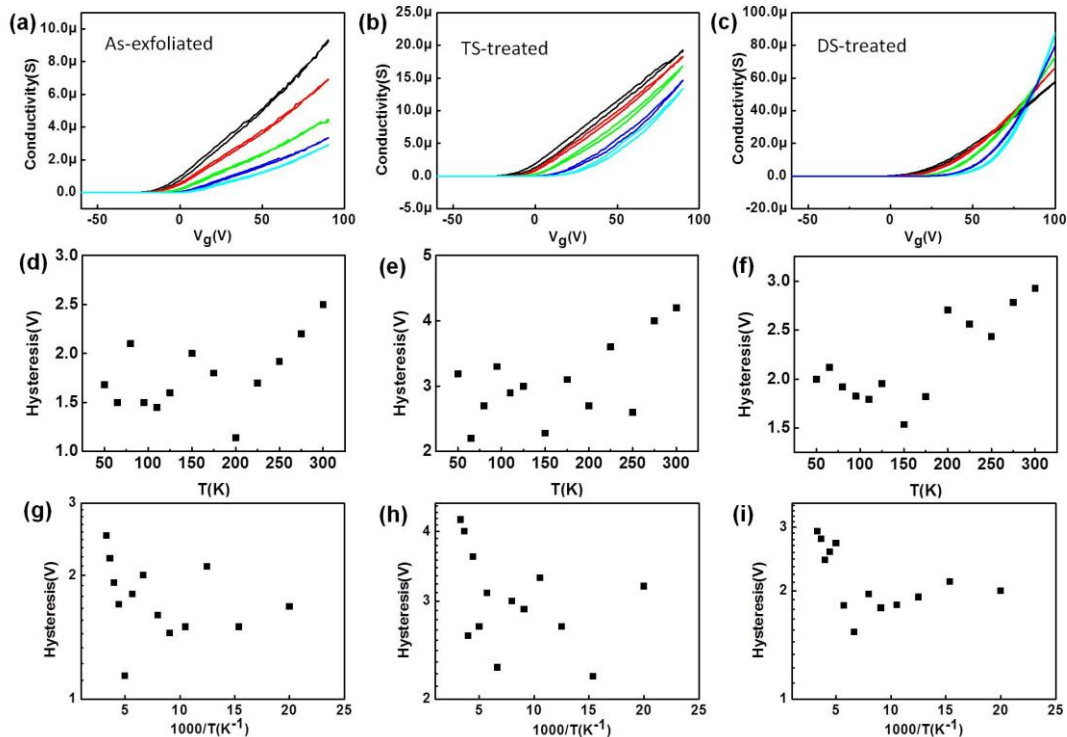
Supplementary Figure 7. (a) (b) Low-magnification TEM images of MoS₂ samples showing the areas with and without organic residue from the transfer process. (c) (d) High-resolution TEM images of clean area and contaminated area, respectively.



Supplementary Figure 8. Low-magnification TEM images of the edge of (a) monolayer (b) 2-layer and (c) 4-layer MoS₂ samples.

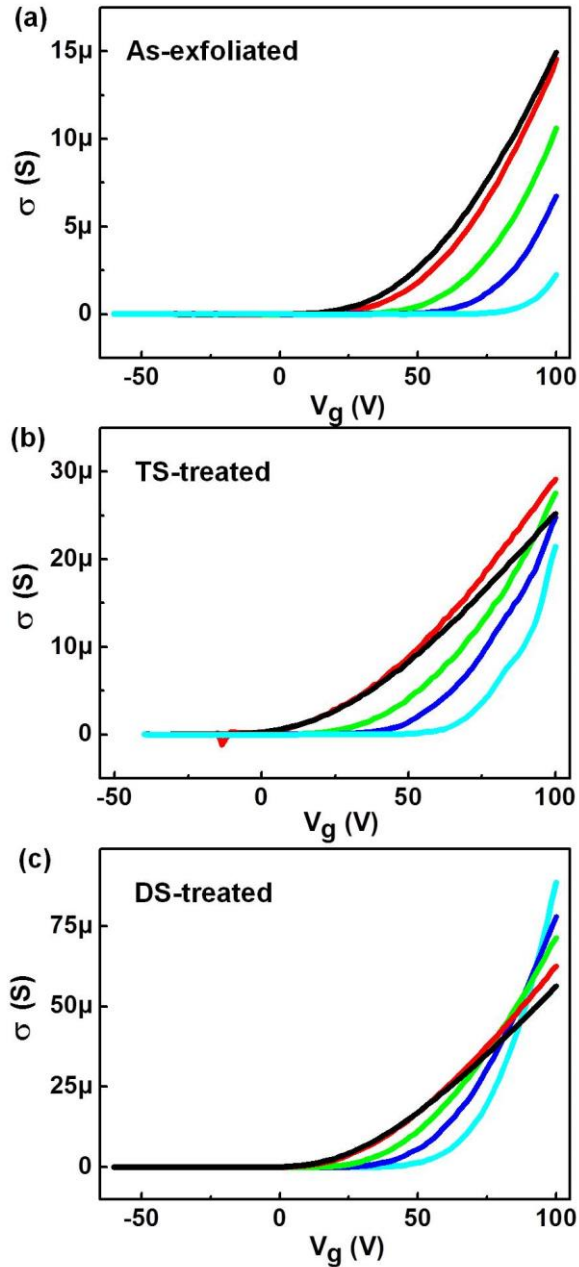


Supplementary Figure 9. (a) TEM image of the TS-treated monolayer MoS₂ in Fig. 2 of main text. Inset shows a low-magnification image of the MoS₂ sample edge confirming its monolayer nature. (b) Intensity profile along lattices with (red) and without (black) a SV. The profiles are taken at the dashed lines in (a). Compared to regular lattice, the SV shows brighter contrast, making it possible to identify them with high accuracy². (c) and (d) are histogram of the density of SV in (c) as-exfoliated and (d) TS-treated monolayer MoS₂. The average density of SV is estimated to be $6.5 \times 10^{13} \text{cm}^{-2}$ and $1.6 \times 10^{13} \text{cm}^{-2}$, respectively. (e) and (f) are the same TEM images of Fig. 2 in main text. A band-pass filter to the Fast Fourier Transformation of the original images and false-colour reconstruction are applied to enhance the visibility of the SV (pointed by white arrows).

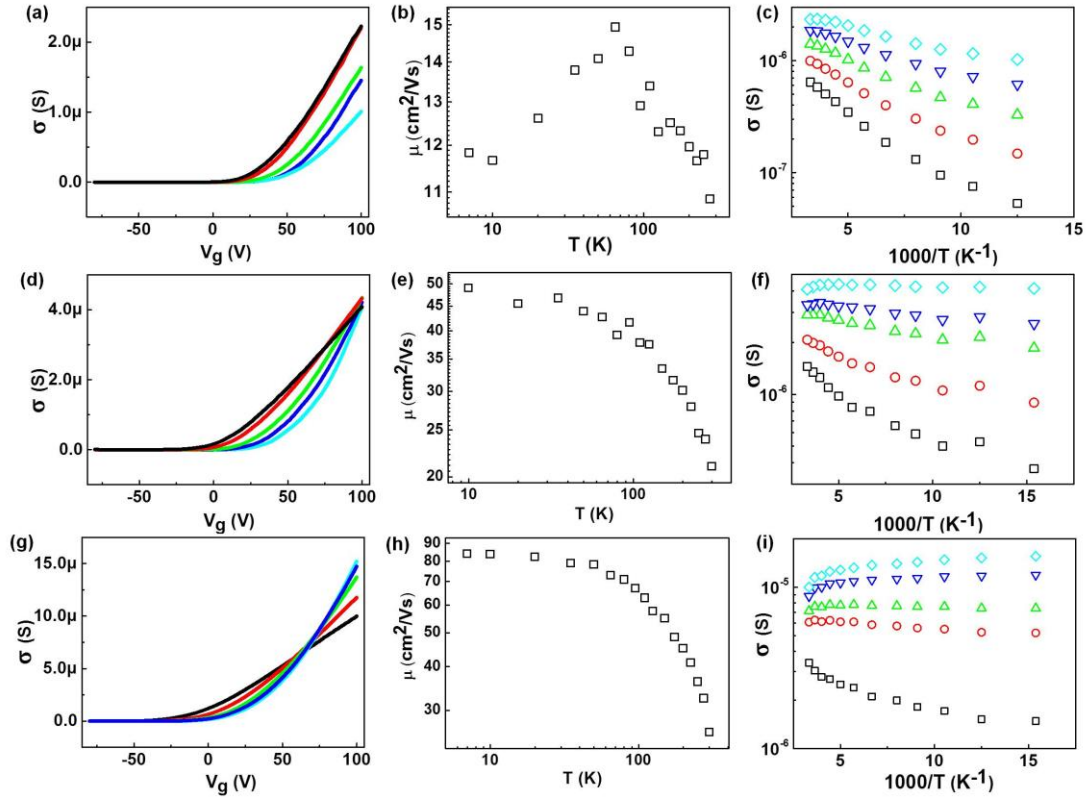


Supplementary Figure 10. Typical double-sweep transfer characteristics of (a) as-exfoliated, (b) TS-treated and (c) DS-treated monolayer MoS₂ devices at different

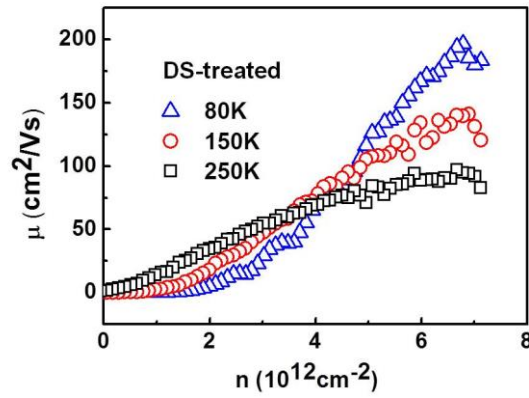
temperatures. Black: 300K, red: 225K, green: 150K, blue: 80K, cyan: 50K. (d)-(f) are the hysteresis as a function of temperature for the three devices respectively. (g)-(i) are the Arrhenius plot of hysteresis for the three devices respectively.



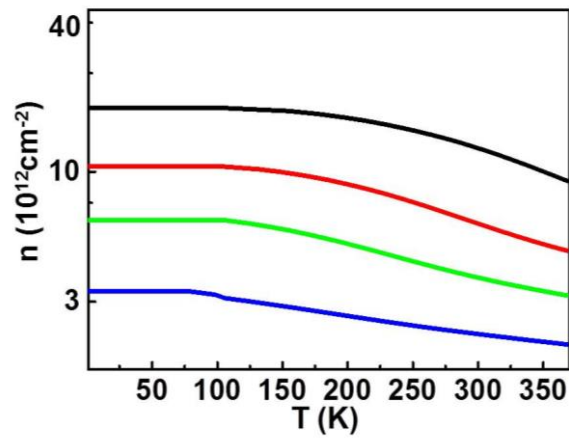
Supplementary Figure 11. Four-probe σ vs V_g characteristics for (a) as-exfoliated, (b) TS-treated, and (c) DS-treated monolayer MoS_2 in Fig. 3. In each panel, black, red, green, blue and cyan curve are taken at $T=300\text{K}$, 250K , 150K , 80K and 20K respectively.



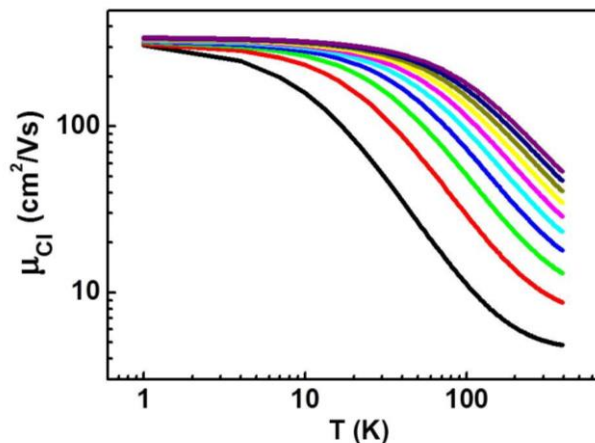
Supplementary Figure 12. Transport data of three additional monolayer MoS₂ devices in two-terminal geometry. (a), (d) and (g) are two-probe σ vs V_g characteristics for the as-exfoliated, TS-treated, and DS-treated monolayer MoS₂ sample respectively. In each panel, black, red, green, blue and cyan curve are taken at $T=300\text{K}$, 250K , 150K , 80K and 20K respectively. (b), (e) and (h) are μ vs T for the as-exfoliated, TS-treated, and DS-treated monolayer MoS₂ sample at $n=7.1 \times 10^{12} \text{cm}^{-2}$. (c), (f) and (i) are Arrhenius plots of σ for the as-exfoliated, TS-treated, and DS-treated monolayer MoS₂ sample respectively. In each panel, from top to bottom, $n=7.0$, 6.0 , 5.0 , 4.0 , $3.0 \times 10^{12} \text{cm}^{-2}$ respectively. The scaling of σ and μ with temperature and carrier density are qualitatively the same as the four-terminal devices discussed in the main text. The absolute values of σ and μ are smaller because of contact resistance.



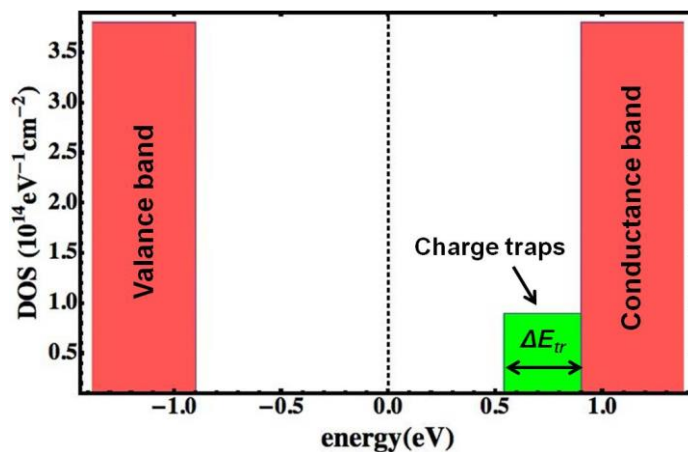
Supplementary Figure 13. μ vs n for the DS-treated sample discussed in the main text at $T=80\text{K}$, 150K and 250K . The mobility edge clearly decreases with temperature.



Supplementary Figure 14. Calculated MIT critical points under different N_{tr} , using the parameters of the DS-treated sample in Table 1 of main text. From top to bottom, $N_{tr}=13.9$, 8.12 , 5.22 and $2.9 \times 10^{12} \text{cm}^{-2}$ respectively. From this figure, we can see that n_0 is roughly proportional to but slightly higher than N_{tr} .



Supplementary Figure 15. Calculated μ_{Cl} as a function of T under $N_i=10^{12}\text{cm}^{-2}$. From bottom to top, n is from $1.0 \times 10^{12}\text{cm}^{-2}$ to $1.0 \times 10^{13}\text{cm}^{-2}$ at a step of $1.0 \times 10^{12}\text{cm}^{-2}$.



Supplementary Figure 16. Density of states of the valance band, conduction band and trap-induced impurity band used in our model.

Supplementary Note 1. After transfer to TEM grid, there are some organic residues on the MoS₂ samples. Usually the contaminations are not everywhere, but only on certain part of a sample. During TEM, we choose the area without contamination to take high-resolution images and analyze the defects. Supplementary Figure 7a and b show low-magnification TEM images of two MoS₂ samples, and we can clearly identify the clean and contaminated areas respectively. In addition, contaminated area looks very different from the clean area in high-resolution images (Supplementary Fig 7c, d),

because the organic contaminations are long chained polymers. Therefore, the observed point defects are not organic contaminations but rather intrinsic defects from MoS₂. In addition, the number of layers can also be easily distinguished under TEM by looking at the sample edges (Supplementary Fig. 8). We always check the monolayer nature of MoS₂ samples before performing high-resolution TEM characterizations.

References:

1. B. Chakraborty, H. S. S. Ramakrishna Matte, A. K. Sood & C. N. R. Rao, Layer-dependent resonant Raman scattering of a few layer MoS₂, *J. Raman Spectrosc.* **44**, 92 (2013).
2. Qiu, H. et al. Hopping transport through defect-induced localized states in molybdenum disulphide. *Nature Comm.* **4**, 2642 (2013).